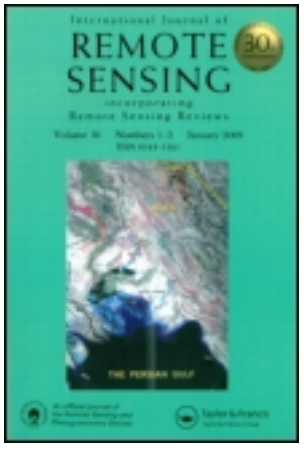

International Journal of Remote Sensing
Publication details, including instructions for authors and subscription information:
http://www.tandfonline.com/loi/tres20

Obtaining global land-surface broadband emissivity from MODIS collection 5 spectral albedos using a dynamic learning neural network

Jie Cheng[a], Shunlin Liang[ab], Y.C. Tzeng[c] & Lixin Dong[a]

[a] State Key Laboratory of Remote Sensing Science, College of Global Change and Earth System Science, Beijing Normal University, Beijing 100875, China

[b] Department of Geographical Science, University of Maryland, College Park 20742, USA

[c] Department of Electronics Engineering, National Lien-Ho College of Technology and Commerce, Maio-Li, Taiwan, ROC

Published online: 17 Feb 2014.

To cite this article: Jie Cheng, Shunlin Liang, Y.C. Tzeng & Lixin Dong (2014) Obtaining global land-surface broadband emissivity from MODIS collection 5 spectral albedos using a dynamic learning neural network, International Journal of Remote Sensing, 35:4, 1395-1416, DOI: 10.1080/01431161.2013.876517

To link to this article: http://dx.doi.org/10.1080/01431161.2013.876517

International Journal of Remote Sensing, 2014
Vol. 35, No. 4, 1395–1416, http://dx.doi.org/10.1080/01431161.2013.876517

Taylor & Francis
Taylor & Francis Group

Obtaining global land-surface broadband emissivity from MODIS collection 5 spectral albedos using a dynamic learning neural network

Jie Cheng[a]*, Shunlin Liang[a,b], Y.C. Tzeng[c], and Lixin Dong[a]

[a]*State Key Laboratory of Remote Sensing Science, College of Global Change and Earth System Science, Beijing Normal University, Beijing 100875, China;* [b]*Department of Geographical Science, University of Maryland, College Park 20742, USA;* [c]*Department of Electronics Engineering, National Lien-Ho College of Technology and Commerce, Maio-Li, Taiwan, ROC*

(*Received 5 April 2013; accepted 4 December 2013*)

Surface broadband emissivity (BBE) is a key parameter for estimating surface radiation budget, but it is treated crudely in land-surface models because of a lack of global-scale observational BBE data. In this study, the non-linear relationship between the BBE that is calculated from the Advanced Spaceborne Thermal Emission and Reflection Radiometer (ASTER) emissivity product and the seven Moderate Resolution Imaging Spectroradiometer (MODIS) narrowband albedos was established individually for bare soils, transition areas, and vegetated areas using a dynamic learning neural network (DLNN). The trained DLNN was tested using a vast array of independent samples, and the results are robust with a bias and root-mean square error (RMSE) of $-1e^{-4}$ and 0.012 for bare soils, $2e^{-4}$ and 0.012 for transition areas, and $7e^{-4}$ and 0.010 for vegetated areas. Two independent field-measured emissivity data sets that were measured over sand dunes were used to validate the DLNN. With respect to the BBE that was calculated from the field-measured emissivities, the bias was 0.019. Ultimately, we introduced the strategy of generating a global land-surface BBE product and presented an example of a global BBE map.

1. Introduction

Broadband emissivity (BBE) is a key parameter for estimating surface longwave net radiation, which is a component of the surface radiation budget and an important parameter for climate, weather, and hydrological models (Sellers et al. 1997; Jin and Liang 2006; Liang et al. 2010; Cheng et al. 2011; Cheng and Liang 2013). A study of the simulated energy balance sensitivity to changes in the emissivity over Northern Africa and the Arabian Peninsula has shown that, on average, a decrease of 0.1 in the soil BBE increased the ground and air temperatures by approximately 1.1°C and 0.8°C, respectively, and decreased the net and upward longwave radiation by approximately 6.6 and 8.1 W m^{-2}, respectively (Zhou, Dickinson, Tian, et al. 2003). The study of Jin and Liang (2006) indicated that the simulation results of climate models were greatly improved by incorporating the satellite-derived BBE. However, because of the lack of adequate observation, a constant emissivity value or very simple parameterizations are adopted in land-surface energy balance studies and general circulation models (Jin and Liang 2006; Zhou, Dickinson, Tian, et al. 2003; Bonan et al. 2002). For example, the National Center for Atmospheric Research (NCAR) Community Land Model Version 2 (CLM2) calculates a canopy emissivity from the leaf

*Corresponding author. Email: brucechan2003@126.com

area index (LAI) and sets the soil and snow emissivities to 0.96 and 0.97, respectively (Bonan et al. 2002).

Generally, there are two methods that can be used to obtain the land-surface BBE. The first method is a classification-based method. Each land-surface type was assigned a constant BBE value that was derived from laboratory-measured emissivity data. For example, Wilber, Kratz, and Gupta (1999) divided the earth's surface into a 10′ × 10′ spatial resolution grid, categorized the land surface into 18 scene types, and generated a global BBE (5–100 μm) map by assigning a constant BBE value to each type that was based on the laboratory-measured spectral data. The second method involves converting existing narrowband emissivity to BBE. The BBE at a certain window (e.g. the 8–13.5 μm spectral range) can be expressed as a linear combination of Advanced Spaceborne Thermal Emission and Reflection Radiometer (ASTER) or Moderate Resolution Imaging Spectroradiometer (MODIS) narrowband emissivities (Ogawa et al. 2002). With this method, Ogawa, Schmugge, and Rokugawa (2008) and Ogawa and Schmugge (2004) mapped the global monthly BBE (8–13.5 μm) using the MODIS emissivity product (approximately 5 km) and a North Africa BBE (8–13.5 μm) that used the ASTER emissivity product (90 m). These two methods share two common drawbacks: (1) The BBE retrieval accuracy is limited. The first method cannot capture the dramatic change in the soil BBE and the BBE seasonal change for vegetated areas. The accuracy of the second method is prone to the uncertainties of current satellite emissivity products. Land surface emissivity (LSE) retrieval from thermal infrared (TIR) radiometric measurements is an ill-posed problem, i.e. solving $N + 1$ variables with N equations (Cheng, Liu, et al. 2008; Liang 2004; Li et al. 2013; Schmugge et al. 2002; Jacob et al. 2004). The solutions of ill-posed problems are sometimes unstable. For example, the V5.0 of the MODIS emissivity product (MOD11B1) was overestimated in all bands with a mean absolute difference of 0.0193 when compared to the lab results (Hulley, Hook, and Baldridge 2009). (2) Either the spatial or temporal resolutions of the derived BBE are limited. The ASTER revisit cycle is 16 days, which makes it impossible to produce a global LSE product on a monthly scale. The spatial resolution of the MODIS narrowband emissivity product that was computed through the day/night algorithm is approximately 5 km. A high-quality BBE data set that has finer spatial and temporal resolutions will be useful for surface energy balance studies on local scales and to validate coarse resolution data, which would improve our understanding of the land–atmosphere interactions (Ogawa and Schmugge 2004; Ogawa, Schmugge, and Rokugawa 2008; Liang 2011).

Tsvetsinskaya et al. (2002) found that the MODIS albedo is largely related to specific soil and geological features in Northern Africa and the Arabian Peninsula, which suggests that surface types can be used to characterize the albedo in those areas (Tsvetsinskaya et al. 2002). Zhou, Dickinson, Ogawa, et al. (2003) showed that the ASTER BBE (in the 3–14 μm spectral range) has a linear relationship with MODIS's seven narrowband and three broadband albedos individually. The study of Ren et al. (2013) indicated that there was a linear relationship between ASTER BBE (8–13.5 μm) and MODIS's seven narrowband albedos as well as NDVI over the relatively homogeneous vegetated areas at a global scale. The contribution of NDVI to the predicted BBE was much smaller compared to that of narrowband albedos. If this linkage between the ASTER BBE and MODIS albedo exists globally for bare soils and vegetated areas, then we can obtain an 8 day 1 km BBE using the MODIS 8 day 1 km albedo product, which enables high spatial-temporal resolution global BBE generation and benefits the studies of the surface radiation budget. The objective of this study was to establish the relationship between the MODIS albedo and the ASTER BBE on a global scale, to help generate a global 8 day 1 km land-surface BBE product from 2000 to 2010. The remainder of this article is

organized as follows. Section 2 provides a detailed description of the data that was used. Section 3 briefly describes the dynamic learning neural network (DLNN) and the scheme for retrieval of the global land-surface BBE. Section 4 presents the retrieval results for bare soils, mixed surfaces, and vegetated surfaces using the DLNN. Section 5 shows the validation results for bare soils. The schemes for generating global BBE products are discussed in Section 6, and a conclusion is provided in Section 7.

2. Data

The satellite data included are (1) the MODIS albedo products (MCD43B3 and MCD43B2), (2) the MODIS normalized difference vegetation index (NDVI) product (MOD13A2), and (3) the ASTER emissivity product (AST05). The temporal and spatial resolutions of the MCD43B3 product are 8 days and 1 km, respectively. There are two types of albedos: white-sky (diffuse) albedo and black-sky (direct) albedo. The seven narrowband black-sky albedos are adopted here. The MODIS NDVI was used to identify different land covers, such as bare soils, transition areas, and vegetated areas. The temporal and spatial resolutions of the NDVI are 16 days and 1 km, respectively. The required auxiliary data are the soil taxonomy and the MODIS land-cover products (MOD12Q1). The former was used to identify different soil orders, and the latter was used to identify different vegetation types. The soil taxonomy map was downloaded from the USDA NRCS (http://www.nrcs.usda.gov/wps/portal/nrcs/detail/soils/use/?cid=nrcs142p2_054013), which is based on a reclassification of the 1994 FAO-UNESCO soil map of the world combined with a soil climate map. The map's spatial resolution is approximately 0.0333°, with 5400 × 10,800 pixels. As shown in Figure 1, there are 12 soil orders in the map. According to the soil taxonomy, we selected the study areas and extracted the samples for training and testing the neural network for bare soils. To extract as many bare soil pixels as possible, we attempted to select relatively large and homogeneous areas as the study area for each soil order. The selected

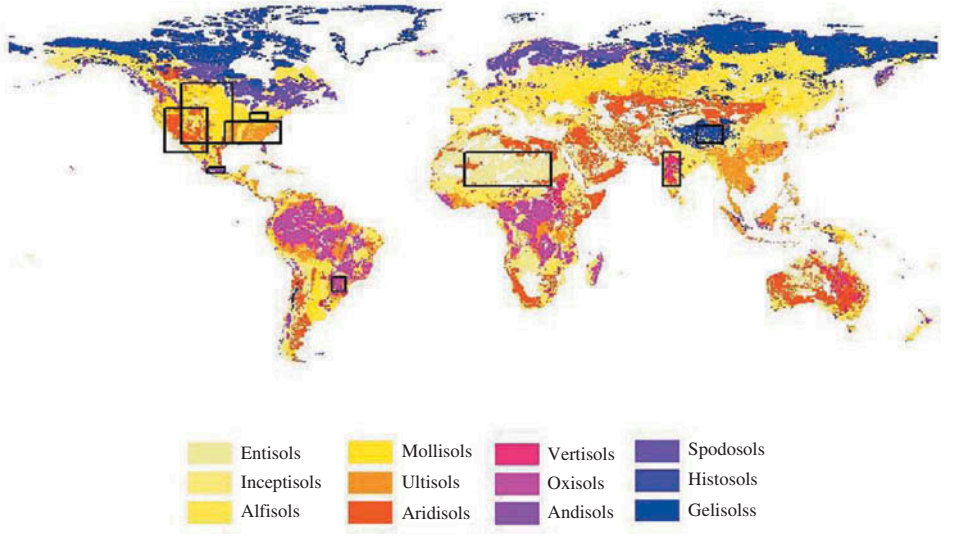

Figure 1. USDA NRCS soil taxonomy and selected study areas. Other classes, such as rocky land, shifting sand, and ice/glacier, are not included in the map.

Table 1. Geographic locations of selected study areas and time intervals for the data that were used.

Soil order	(Lat)/(Lon)	Time interval
Alfisols	(38.67° to 41.77°)/(–86.7° to –80.03°)	January 2009 to March 2009; January 2007 to March 2007
Andisols	(18.3° to 20.7°)/(–103.3° to –96.7°)	February 2009 to March 2009; January 2008 to March 2008
Aridisols	(26.7° to 43.4°)/(–120° to –103.3°)	January 2009 to February 2009; January 2008 to March 2008
Entisols	(13.3° to 26.7°)/(–3.3° to 30°)	February 2009 to February 2009; January 2008 to February 2008
Gelisols	(30.03° to 36.7°)/(86.63° to 96.63°)	January 2008 to January 2008; January 2009 to April 2009
Inceptisols	(30.03° to 36.7°)/(86.63° to 96.63°)	January 2008 to January 2008; January 2009 to April 2009
Mollisols	(30° to 53.4°)/(–113.3° to –93.4°)	March 2009 to March 2009; January 2008 to March 2008
Oxisols	(to27.5° to to22°)/(–55° to –50°)	July 2008 to September 2008; January 2009 to January 2010
Ultisols	(30° to 38.4°)/(–96.7° to –75°)	October 2008 to February 2009; January 2007 to April 2007
Vertisols	(13.3° to 26.7°)/(73.3° to 80°)	February 2009 to March 2009; January 2008 to March 2008

study areas are shown in Figure 1. For the soil orders of histosols and spodosols, we tried several places and time intervals but did not find bare soil pixels. We found it difficult to locate bare soil pixels at high latitudes and in equatorial zones. Table 1 presents the geographical locations of the selected study areas and the time intervals of the data used. The MOD12Q1 is a yearly L3 Global 1 km SIN Grid product, which incorporated five different land-cover classification schemes. The International Geosphere Biosphere Programme (IGBP) global vegetation classification scheme was used to discriminate vegetated and non-vegetated land covers. Based on the MOD12Q1, we selected 49 sites from the sites of the MODIS land subsets. Among them, 40 sites were used to train the neural network and 9 sites were used to test the trained neural network. The land cover of both the training and test sites includes cropland, forest, grassland, savannas, and shrublands. Figure 2 shows the distribution of these sites. All of the matched clear-sky satellite data that range from 2000 to 2010 were downloaded.

3. Methods

A neural network is an interconnection of simple computational elements, or nodes, with activation functions that are usually non-linear, monotonically increasing, and differentiable (Blackwell 2005). Without any *a priori* knowledge of the data distribution and the relationship between the input variables and output variables, a neural network can directly establish a relationship between the input variables and output variables from the training ensembles. Furthermore, a neural network that has only a single hidden layer with a sufficient number of nodes with non-linear activation functions is capable of approximating any real-valued continuous scalar function to a given precision over a finite domain (Hornik, Stinchcombe, and White 1989). Thus, a neural network is a powerful tool for solving non-linear problems. A neural network has been successfully

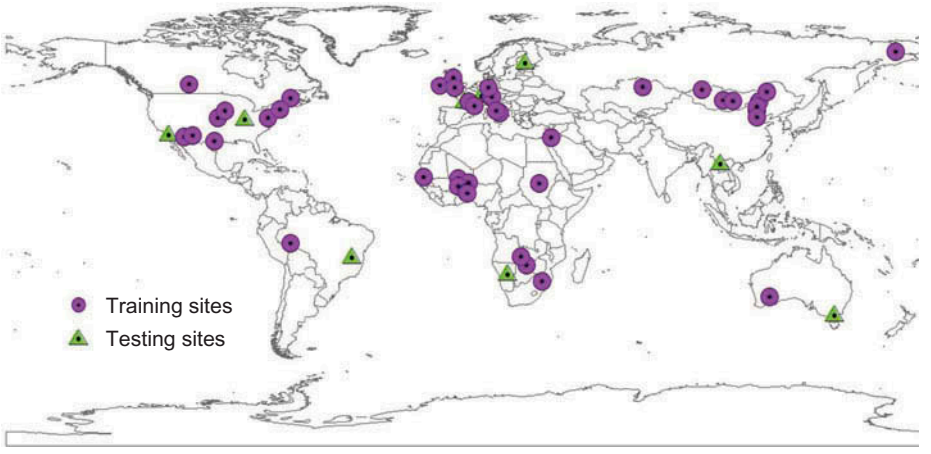

Figure 2. Distribution of sites used for training and testing the neural network for vegetated areas.

applied to parameter inversion in remote sensing, such as atmospheric composition retrieval (Blackwell 2005; Aires et al. 2002; Turquety, Hadji-Lazaro, and Clerbaux 2002) and land-surface parameter retrieval (Cheng, Xiao, et al. 2008; Mao et al. 2008; Smith 1993; Fang and Liang 2003; Jin and Liu 1997; Tang et al. 1992; Tedesco et al. 2004; Chen, Kao, and Tzeng 1995; Baret et al. 2007), which are strongly non-linear problems. Regarding the specific land-surface parameter inversion problem, the accuracy of a neural network can be better than that of physically based algorithms. For example, the uncertainty of the global CYCLOPES LAI that was computed using the neural network is better than MODIS and (GLOBCARBON) LAI (computed by a physically based algorithm) (Fang et al. 2012).

We selected the DLNN (Tzeng et al. 1994; Chen, Kao, and Tzeng 1995) to obtain the BBE from the MODIS albedos in this study. The DLNN was, in fact, a modified multi-layer perceptron (MLP) in structure, and the Kalman filtering technique was used in its learning process. The DLNN has the features of global minimization, convergence warranty, and built-in optimization of a weighting function at little expense to computer storage (Liou, Tzeng, and Chen 1999). An MLP neural network is composed of one input layer, one output layer, and one or more hidden layers in between. A neuron is the basic element of a neural network. The output signal y for a neuron can be expressed as

$$h = \mathbf{w}^{\mathrm{T}}\mathbf{x} + \varphi, \tag{1}$$

$$y = \mathrm{S}(h), \tag{2}$$

where h is the activation, $\mathbf{w} = [w_1 w_2 \ldots w_n]^{\mathrm{T}}$ is an $n \times 1$ weight vector, the superscript T denotes the transpose operation, $\mathbf{x} = [x_1 x_2 \ldots x_n]^{\mathrm{T}}$ is an $n \times 1$ input vector, φ is an additive bias, and S is an activation function. Assuming that there are n input nodes at an input layer, m output nodes at an output layer, and p layers of hidden layers that have n_i nodes at the hidden layer i, the input of the neural network $\mathbf{x} = [x_1 x_2 \ldots x_n]^{\mathrm{T}}$ is an $n \times 1$ input vector, and the output of the neural network $\mathbf{y} = [y_1 y_2 \ldots y_m]^{\mathrm{T}}$ is an $m \times 1$ output vector. We have $\mathbf{x} = \mathrm{S}(\mathbf{h}_0)$ and $\mathbf{y} = \mathrm{S}(\mathbf{h}_{p+1})$ if we let $n = n_0$ and $m = n_{p+1}$. The output that is generated

from a set of input signals at each layer can be computed according to the following recursive formula for $i = 1, 2, ..., p + 1$

$$\mathbf{h}_i = \mathbf{W}_i \mathrm{S}(\mathbf{h}_{i-1}) + \mathbf{\Phi}_i, \tag{3}$$

where $\mathbf{\Phi}_i = [\varphi_{i1}\varphi_{i1}...\varphi_{in_i}]^{\mathrm{T}}$ is an $n_i \times 1$ bias vector, $\mathbf{h}_i = [h_{i1}h_{i1}...h_{in_i}]^{\mathrm{T}}$ is an $n_i \times 1$ activation vector, $\mathrm{S}(\mathbf{h}_i) = [S(h_{i1})S(h_{i2})...S(h_{in_i})]^{\mathrm{T}}$ is an $n_i \times 1$ signal vector, and $\mathbf{W}_i = [\mathbf{w}_{i1}\mathbf{w}_{i2}...\mathbf{w}_{in_i})]^{\mathrm{T}}$ is an $n_i \times n_{i-1}$weight matrix, whereas the $1 \times n_{i-1}$ weight vector at layer i is defined as $\mathbf{w}_{ij} = [w_{ij1}w_{ij2}...w_{ijn_{i-1}}]^{\mathrm{T}}$. The notations are defined as

φ_{ij}, bias of the jth node at layer i.
h_{ij}, activation of the jth node at layer i.
$\mathrm{S}(h_{ij})$, output signal of the jth node at layer i.
w_{ijk}, weight connected between the jth node at layer i and the kth node at layer $i - 1$.

By taking two modifications: (1) every node in the input layer and in all of the hidden layers was fully connected to the output layer; and (2) the activation function was removed from each output layer. The output of the modified network can be expressed by the weighted sum of the polynomial basis vectors

$$\mathbf{y} = \underline{\mathbf{W}}\underline{\mathbf{x}}, \tag{4}$$

where $\underline{\mathbf{W}} = [\underline{\mathbf{w}}_1\underline{\mathbf{w}}_2...\underline{\mathbf{w}}_m]^{\mathrm{T}}$ is an $m \times M$ weight matrix. Whereas the $1 \times M$ long weight vector is defined as $\underline{\mathbf{w}}_k = [\underline{\mathbf{w}}_{0k}|\underline{\mathbf{w}}_{1k}|...|\underline{\mathbf{w}}_{ik}|...|\underline{\mathbf{w}}_{pk}|\varphi_{p+1,k}]$, the $1 \times n_i$ weight vector is defined as $\underline{\mathbf{w}}_{ik} = [\underline{w}_{i1k}\underline{w}_{i2k}...\underline{w}_{in_ik}]$, and $\underline{\mathbf{w}}_{ijk}$ is the weight connected between the jth node in layer i and the kth node in the output layer. This linearization allowed the use of the Kalman filtering technique to update the weights during the learning process. Each updated estimate of the neural network weight is computed from the previous estimate and the new input data. The weight connected to each output node can be updated independently, and the original problem can therefore be decomposed into m scalar problems: for $k = 1, 2, ..., m$

$$y_k = \underline{\mathbf{w}}_k\underline{\mathbf{x}}. \tag{5}$$

Using the Kalman filtering technique, Equation (5) can be modelled in the form

$$d_k^j = \underline{\mathbf{w}}_k^j\underline{\mathbf{x}} + v_k^j, \tag{6}$$

$$\underline{\mathbf{w}}_k^{j+1} = \underline{\mathbf{w}}_k^j\mathbf{A}^j + \mathbf{u}_k^j\mathbf{B}^j, \tag{7}$$

where the superscript j denotes the added jth training pattern, $\mathbf{A}^j$ is an $M \times M$ state transition matrix, $\mathbf{B}^j$ is an $M \times M$ diagonal matrix, $\mathbf{u}_k^j$ represents a $1 \times M$ process error vector, and v_k^j is a scalar measurement error. The update of the network weights is made according to the following recursions, for $j = 1, 2, ..., N$

$$\hat{\underline{\mathbf{w}}}_k^j = \tilde{\underline{\mathbf{w}}}_k^j + \mathbf{g}_k^j[d_k^j - \tilde{\underline{\mathbf{w}}}_k^j\underline{\mathbf{x}}], \tag{8}$$

$$\tilde{\underline{\mathbf{w}}}_k^{j+1} = \hat{\underline{\mathbf{w}}}_k^j\mathbf{A}^j, \tag{9}$$

where $\tilde{\underline{\mathbf{w}}}_k^j$ is the one-step predicted estimate, $\hat{\underline{\mathbf{w}}}_k^j$ is the filter estimate of $\underline{\mathbf{w}}_k^j$, and $\mathbf{g}_k^j$ is the computed Kalman gain. The computed Kalman gain can be viewed as an adaptive learning rate and is computed according to the following steps

$$\mathbf{g}_k^j = (\tilde{\mathbf{P}}_k^j \underline{\mathbf{x}})^{\mathrm{T}} [\underline{\mathbf{x}}^{\mathrm{T}} \tilde{\mathbf{P}}_k^j \underline{\mathbf{x}} - \upsilon_k^j]^{-1}, \tag{10}$$

$$\hat{\mathbf{P}}_k^j = \tilde{\mathbf{P}}_k^j - \mathbf{g}_k^{j\,\mathrm{T}} (\tilde{\mathbf{P}}_k^j \underline{\mathbf{x}})^{\mathrm{T}}, \tag{11}$$

$$\hat{\mathbf{P}}_k^{j+1} = \mathbf{A}^{j\mathrm{T}} \hat{\mathbf{P}}_k^j \mathbf{A}^j + \mathbf{B}^{j\mathrm{T}} \mathbf{Q}_k^j \mathbf{B}^j, \tag{12}$$

where $\tilde{\mathbf{P}}_k^j = \mathrm{E}[(\underline{\mathbf{w}}_k^j - \tilde{\underline{\mathbf{w}}}_k^j)^{\mathrm{T}} (\underline{\mathbf{w}}_k^j - \tilde{\underline{\mathbf{w}}}_k^j)]$ and $\hat{\mathbf{P}}_k^j = \mathrm{E}[(\underline{\mathbf{w}}_k^j - \hat{\underline{\mathbf{w}}}_k^j)^{\mathrm{T}} (\underline{\mathbf{w}}_k^j - \hat{\underline{\mathbf{w}}}_k^j)]$ are the one-step predicted and filter estimate error covariance matrices, respectively.

The scheme for retrieving the global land-surface BBE is shown in Figure 3. The ASTER 90 m emissivity product was aggregated to 1 km by averaging the values of ASTER pixels that fall into the field of view (FOV) of a MODIS 1 km pixel to match the spatial resolution of the MODIS albedo and the NDVI. Good quality and clear sky data were extracted based on their respective quality control (QC) data. For example, only albedo with good quality (full BRDF inversions) was used. Many studies (Ogawa, Schmugge, and Rokugawa 2008; Liang 2004; Wang et al. 2005; Tang et al. 2011; Ogawa et al. 2002) have shown that the BBEs within the 3–14 μm spectral domain can be represented by a linear function of either the ASTER or the MODIS narrowband emissivities, such as Equation (13)

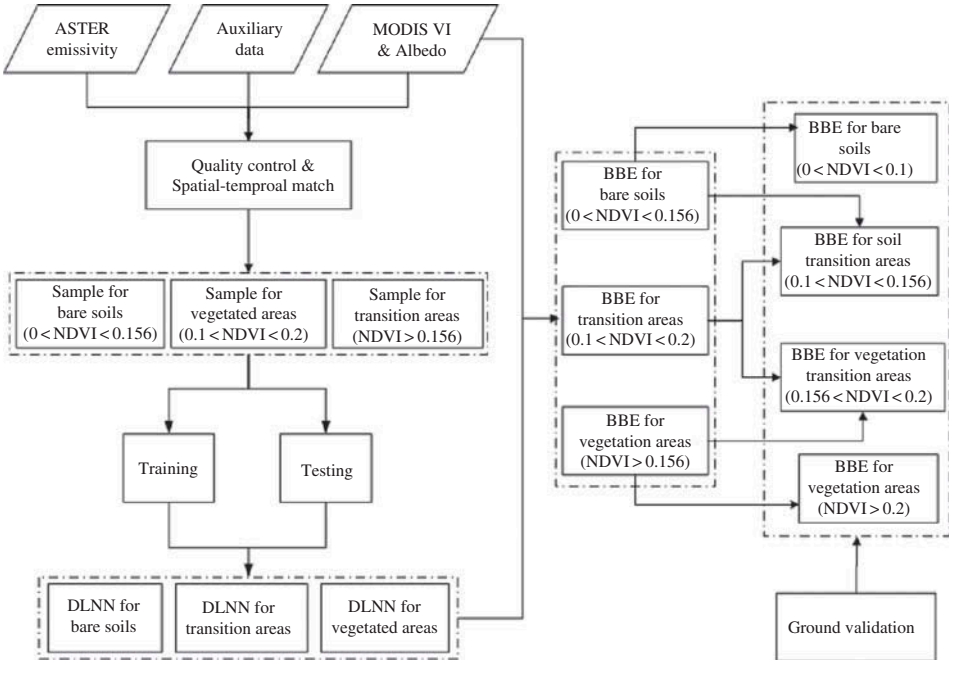

Figure 3. Scheme for retrieving the global land-surface BBE from the MODIS albedo product.

$$\varepsilon_{bb} = \text{const} + \sum_{i=1}^{N} a_i \varepsilon_i, \tag{13}$$

where ε_{bb} is the BBE, N is the number of narrowband, ε_i is the ith narrowband emissivity, and a_i is the coefficient. With the approximately 1–200 μm emissivity spectra of various surface types simulated by modern radiative transfer models, Cheng et al. (2013) found that the BBE in the 8–13.5 μm spectral domain is the most appropriate for calculating the surface longwave net radiation, and they derived the corresponding linear conversion formula. Therefore, the BBE in the 8–13.5 μm spectral domain was calculated from the ASTER five narrowband emissivities using their formula in this study. Table 2 shows the TIR bands and their spectral ranges for the ASTER, and Table 3 presents the coefficients for calculating the ASTER BBE in the 8–13.5 μm spectral domain. Because of the different emissivity spectra features, we classified the global land-surface into four types: water, snow/ice, bare soils, and vegetated areas. Bare soils and vegetated areas were determined according to the NDVI threshold that was used by a previous study (Momeni and Saradjian 2007); a bare soil pixel was identified as $0 < \text{NDVI} < 0.156$ and a vegetated pixel was identified as $\text{NDVI} \geq 0.156$. Misclassification can incur step discontinuities when generating a global land-surface BBE product in sparsely vegetated areas because it is difficult to determine whether the pixel corresponds to bare soils or vegetated areas. We propose setting a transition area to mitigate the BBE difference between the bare soils and the vegetated areas, using an NDVI threshold. In this study, pixels with NDVI values that ranged from 0.1 to 0.2 were labelled as transition areas. Overall, the global land surface was divided into five types is this study. We extracted the samples (Albedo–BBE pairs) for bare soils, transition areas, and vegetated areas, and we developed the corresponding DLNNs with these samples. Then, the developed DLNNs were used to obtain the BBE for bare soils, transition areas, and vegetated areas. Note that there is overlap between the bare soils and transition areas as well as between transition areas and vegetated areas. In the generation of global land-surface BBE, the BBE of the pixels located in the transition areas is the weighted average of their affiliations and depends on the NDVI of the pixels. If the NDVI is between 0.1 and 0.156, its BBE is the average of those calculated by the method for the bare soils and transition areas; if the NDVI lies between 0.156 and 0.2, its BBE is the average of those calculated by the method for the transition areas and vegetated areas. The data extracted from the study areas listed in Table 1 were

Table 2. ASTER TIR bands and their spectral ranges. B_{10}–B_{14} represent the five ASTER TIR bands.

Bands	B_{10}	B_{11}	B_{12}	B_{13}	B_{14}
Spectral range (μm)	8.125–8.475	8.475–8.825	8.925–9.275	10.25–10.95	10.95–11.65

Table 3. Coefficients for calculating the BBE in the 8–13.5 μm spectral domain using the ASTER narrowband emissivity product.

Constant	B_{10}	B_{11}	B_{12}	B_{13}	B_{14}	RMSE	R^2
0.197	0.025	0.057	0.237	0.333	0.146	0.005	0.983

used for bare soils and transition areas, and the data corresponding to the sites that are displayed in Figure 2 were used for vegetated areas.

4. Results

The accuracy of BBE retrieval was characterized by two indices: bias and root-mean-square error (RMSE), which are defined as follows:

$$\text{bias} = \sum_{i=1}^{N} (\text{BBE}_{i,\text{inv}} - \text{BBE}_{i,\text{true}})/N, \tag{14}$$

$$\text{RMSE} = \sqrt{\sum_{i=1}^{N} (\text{BBE}_{i,\text{inv}} - \text{BBE}_{i,\text{true}})^2/(N-1)}, \tag{15}$$

where $\text{BBE}_{i,\text{inv}}$ is the computed BBE, $\text{BBE}_{i,\text{true}}$ is the true BBE, and N is the total number of samples.

4.1. Bare soil

A total of 117,762 samples were extracted from the study areas. The samples for each soil order were randomly split into two parts; part one had 70% samples and part two had 30% samples. In part one, all of the soil orders were combined together for training the DLNN, and in part two, all of the soil orders were combined together for testing the trained DLNN. By proper selection via trial and error, the structure of the DLNN was set at 7-50-50-1, which means that seven nodes represent the MODIS black-sky albedos in the input layer, each of the two hidden layers has 50 nodes, and one node at the output layer represents the output BBE. Figure 4 compares the ASTER BBE and that predicted by the DLNN for bare soils. The points for each soil order were distributed around the 1:1 line. The bias is $-7e^{-6}$, and the RMSE is 0.011. The bias and the RMSE for each soil order were also calculated and are listed in Table 4. Although the maximum bias is 0.007, the absolute bias for more than half of the soil orders is less than 0.005. The maximum RMSE is 0.014, and the RMSE for the remaining nine soil orders is approximately 0.010. Figure 5 shows a histogram of the differences in the results for the test set. The BBE predicted by the DLNN was in good agreement with the ASTER BBE. Overall, the bias is $-1e^{-4}$, and the RMSE is 0.012. The maximum absolute bias and the RMSE are 0.008 and 0.019, respectively. The test results indicated that the DLNN can be used to obtain the BBE for bare soils.

4.2. Transition areas

The structure of the DLNN for the transition areas was set to that for bare soils as a result of trial and error. In total, 107,581 samples were extracted from the study areas.

Using the method that was adopted in Section 4.1, 70% of the samples were extracted for training the DLNN, and 30% of the samples were extracted for testing the trained DLNN. Figure 6 shows the comparison between the ASTER BBE and that predicted by the DLNN for transition areas. The bias is $-1e^{-6}$ and the RMSE is 0.010. The bias and RMSE for each soil order were also calculated as listed in Table 5. Although the maximum bias is 0.008, the absolute bias for most of the soil orders is less than 0.004.

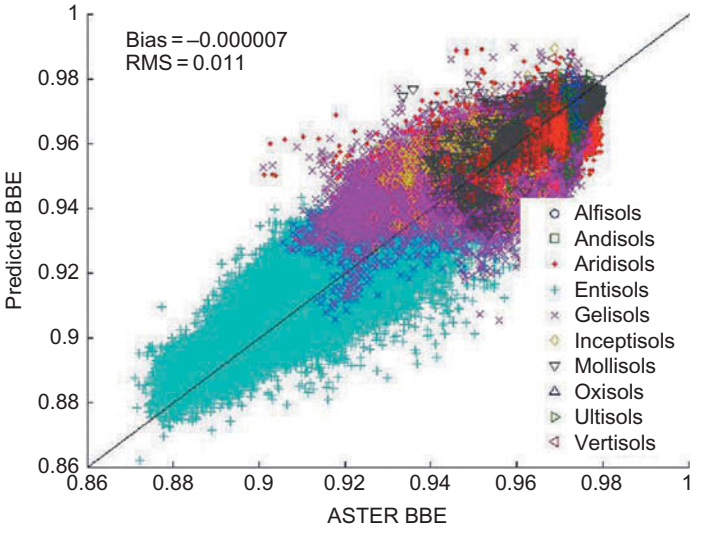

Figure 4. Scatter plot of the BBE calculated by the ASTER narrowband emissivities *versus* that predicted by the DLNN for bare soils.

Table 4. The bias and RMSE for each soil order of bare soil.

Soil order	Bias	RMSE
Alfisols	−0.006	0.011
Andisols	−0.005	0.012
Aridisols	−0.001	0.010
Entisols	0.001	0.009
Gelisols	−0.001	0.011
Inceptisols	0.006	0.014
Mollisols	−0.001	0.006
Oxisols	−0.007	0.012
Ultisols	−0.005	0.014
Vertisols	−0.004	0.008

The maximum RMSE is 0.013, and the RMSE for the remaining nine soil orders is approximately 0.010. The result is shown in Figure 7. The distribution of the differences is similar to that in Figure 5. They all lie in the narrow range of [–0.06, 0.06]. This finding could result from two reasons: (1) as mentioned in Section 4.1, the established non-linear relationship for bare soil is accurate. The NDVI range for bare soils and transition zones was overlapping, which means that we can derive better results by the DLNN for the overlapped part; and (2) the DLNN can establish a non-linear relationship for the land surface whose NDVI lines are between 0.156 and 0.2. The statistical results for the transition zones are also similar to that for bare soils. As a whole, the bias is $2e^{-4}$ and the RMSE is 0.012. The maximum absolute bias and RMSE are 0.007 and 0.016, respectively, which are slightly smaller than that for bare soils. For this reason, the difference histogram for the transition zones is slightly narrower than that for the bare soils. Both the bias and the RMSE are acceptable. Thus, the DLNN can be used to obtain the BBE for the transition areas.

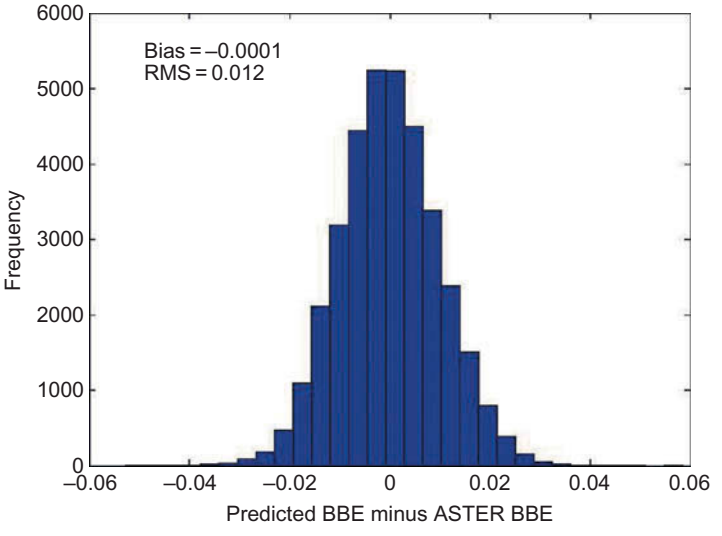

Figure 5. Difference histograms of the ASTER BBE and that predicted by the DLNN for bare soils.

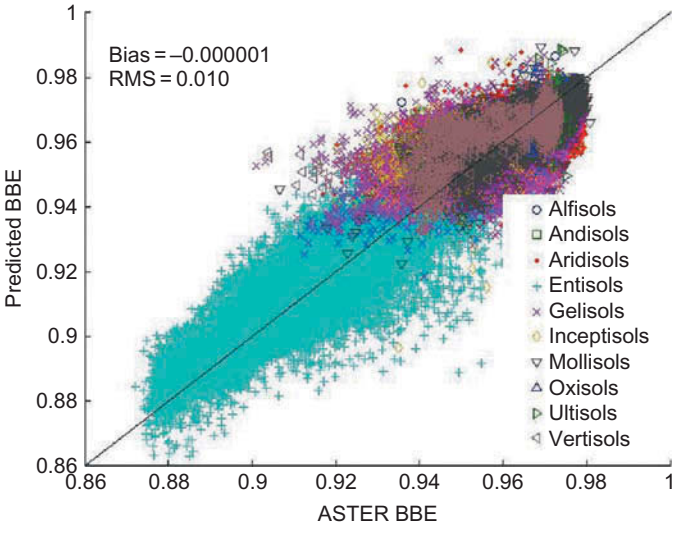

Figure 6. Scatter plot of the BBE calculated by the ASTER narrowband emissivities *versus* that predicted by the DLNN for transition areas.

4.3. Vegetated areas

The structure of the DLNN for the vegetated areas was set to 7-50-50-1 through trial and error. In total, we obtained approximately 1,200,000 samples for training the DLNN. The training result is shown in Figure 8. Obviously, the ASTER BBE for the vegetated areas spans a broad range from approximately 0.85 to 0.99. The DLNN can reproduce this variation range. As is apparent, the divergence of the scatter plot was higher than those for the bare soils and

Table 5. The bias and RMSE for each soil order of transition areas.

Soil order	Bias	RMSE
Alfisols	0.004	0.009
Andisols	0.008	0.013
Aridisols	−0.001	0.009
Entisols	0.001	0.009
Gelisols	0.000	0.009
Inceptisols	0.006	0.013
Mollisols	−0.001	0.006
Oxisols	0.001	0.011
Ultisols	−0.002	0.012
Vertisols	0.003	0.010

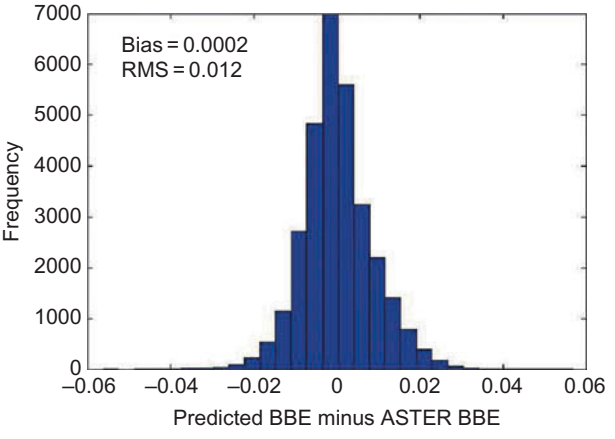

Figure 7. Difference histogram of the ASTER BBE and that predicted by the DLNN for transition areas.

transition areas (see Figures 4 and 6). As seen from Figure 8, the divergence of the samples is also significant when the ASTER BBE is larger, except for the samples at the rightmost with a deep colour. This finding can be ascribed to the larger BBE variations in the vegetation itself. When the NDVI is larger than 0.461, the vegetated surface can be considered fully vegetated (Momeni and Saradjian 2007). The ASTER BBE for fully vegetated samples is 0.967 ± 0.008 in this study. The bias is $2e^{-5}$, which is slightly larger than the results for the bare soils and transition areas, and the RMSE is 0.0095. The DLNN was tested by approximately 400,000 samples. The result is shown in Figure 9. The BBE difference ranges from approximately –0.08 to 0.08, whereas most of the differences lie in the range of [–0.02, 0.02]. This result is consistent with that in Figure 8. The divergences result in larger BBE differences, and good performance of the DLNN brings a narrow distribution to the BBEs difference. The bias and RMSE are $7e^{-4}$ and 0.010, respectively, which means that the DLNN was adapted to obtain the BBE for the vegetated areas.

5. Validation

Validating the emissivity obtained from satellite remote-sensing data is quite complex because the pixels are mixed and non-isothermal under most natural conditions,

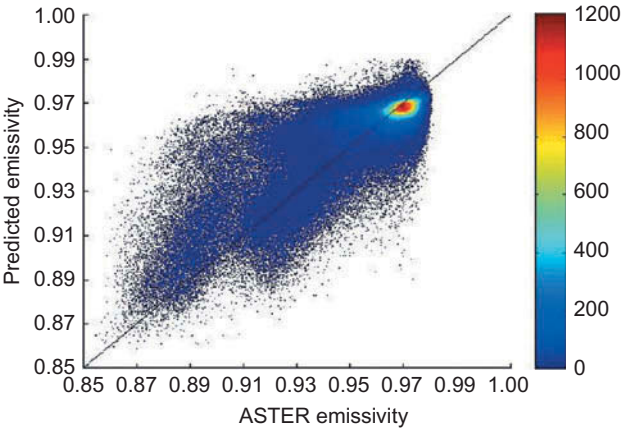

Figure 8. Scatter plot of the BBE calculated by the ASTER narrowband emissivities *versus* that predicted by the DLNN for vegetated areas.

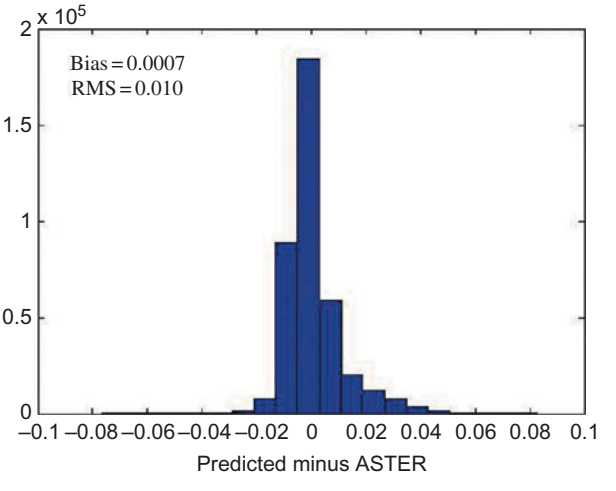

Figure 9. Difference histograms of the ASTER BBE and those predicted by the DLNN for vegetated areas.

especially at moderate or coarse spatial resolutions. Flat and homogeneous land surfaces, such as large water bodies, sands, and grasslands, are always selected as the validation sites. However, visually homogenous sites are not necessarily isothermal in the infrared spectral domain. To our knowledge, the field-measured emissivity at a 1 km spatial resolution is currently unavailable. The field-measured emissivity for vegetated areas is extremely limited. Fortunately, some authors have performed field measurements over homogeneous areas to validate the ASTER 90 m emissivity products (Hulley, Hook, and Baldridge 2009; Sabol et al. 2009). These measurements can be used to validate the BBE estimation method if the validation sites are large enough. For example, when Hulley and Hook (Hulley, Hook, and Baldridge 2009) measured the *in situ* sands' emissivity, they found that large sand dunes have consistent and homogeneous mineralogy and physical properties over long time periods. They conducted five separate field

campaigns to collect sand samples at nine sand dunes in the spring and early summer of 2008. The emissivity spectra of the collected samples were measured in a laboratory using a Nicolet 520 FT-IR spectrometer equipped with a Labsphere integrating sphere (Baldridge et al. 2009). The ASTER narrowband emissivities were derived by convolving the laboratory-measured emissivity spectra with the ASTER TIR spectral response functions. The mineralogy of each dune site was also measured by X-ray diffraction (XRD). More details on the dune sites can be found in their paper. Five relatively large and homogeneous dune sites were selected to validate the trained DLNN for bare soils. Each of the selected dune sites was of the aridisol soil order. The spatially matched ASTER emissivity product and the MODIS albedo product, starting from March 2008 and ending in June 2008, were also downloaded. In total, we completed nine ASTER imageries for both Algodones and Great Sands, eight ASTER imageries for Kelso and Little Sahara, 10 ASTER imageries for Stovepipe Wells, and 34 ASTER imageries for White Sands. For each dune site, the derived narrowband emissivity and downloaded ASTER narrowband emissivity were converted to the BBE in the 8–13.5 spectral range using the converting coefficients provided in Table 3, and the results were compared with the BBE that was calculated from the DLNN. Table 6 presents the difference between the computed BBE and the *in situ* BBE and the difference between the computed BBE and the ASTER BBE. The computed BBE agreed well with the ASTER BBE, and it had an average difference of 0.007. This result is consistent with the comparison results for bare soils presented in Section 4.1. The difference between the computed BBE and the *in situ* BBE was 0.019.

We also conducted a field campaign to validate the new algorithm that was proposed in this article in June 2011. The validation site is located in the central part of the Taklimakan Desert at Xinjiang Province of China, which is the largest active desert in China and the second largest in the world. The Model 102 Portable Field Spectrometer and a Labsphere gold plate were used to measure the spectral radiance emitted by the target and the environment under clear sky. The emissivity spectrum was derived from the radiometric measurements by the iterative spectrally smooth temperature and emissivity separation (ISSTES) algorithm. For each site, we conducted three measurements; then, we randomly chose three points within a distance of approximately 500 m from the site and conducted three measurements at each point. The derived 12 emissivity spectra were averaged and regarded as the emissivity of the site. The average emissivity was converted into BBE in the 8–13.5 spectral range. In total, we obtained BBE at two sites. The BBEs were 0.915 and 0.913 and the BBEs that were computed by the new algorithm were 0.931 and 0.935, respectively. The average difference between the computed BBE and the *in situ* BBE was 0.019. At this stage, we obtained only the

Table 6. BBE difference between the computed BBE and the *in situ* BBE as well as that between the computed BBE and the ASTER BBE.

Dune sites	*In situ*	ASTER	Retrieved	Retrieved – *in situ*	Retrieved – ASTER
Algodones	0.906	0.900	0.919	0.013	0.019
Great Sands	0.924	0.946	0.943	0.019	−0.003
Kelso	0.907	–	0.931	0.024	–
Little Sahara	0.914	0.947	0.943	0.029	−0.004
Stovepipe Wells	0.936	0.930	0.945	0.009	0.015
Taklimakan desert site1	0.915	–	0.931	0.016	–
Taklimakan desert site2	0.913	–	0.935	0.022	–

validation data for bare soil in this study; the collection of more *in situ* data and more extensive field campaigns are under way.

6. Global BBE mapping

The MODIS standard products, the MODIS NDVI data (MOD13A2), and the MODIS albedo products (MCD43B3 and MCD43B2) are required to generate the global land-surface BBE. The land surface was divided into five types: water, snow/ice, bare soils ($0 < \text{NDVI} \leq 0.156$), vegetation areas ($\text{NDVI} \geq 0.156$), and transition areas ($0.1 < \text{NDVI} < 0.2$). Different methods were adopted to determine their BBE. The emissivity spectrum of smooth water surface can be simulated with the Fresnel equation (Born and Wolf 1999), given its refractive index. Figure 10 shows the simulated pure water emissivity spectrum, together with the emissivity spectra in the ASTER spectral library and the MODIS UCSB spectral library. The measured emissivity spectra are distributed in a very narrow band and agree well with the simulated emissivity spectrum. The BBE of water in the ASTER spectral library is 0.984 for all three samples, and the value in the MODIS UCSB spectral library is 0.985 for all five samples. The BBE of water was specified as 0.985 in the generation of the global land-surface BBE. Regarding snow and ice, we can use the radiative transfer model and the Fresnel equation to simulate their emissivity spectra (Cheng et al. 2010). However, it is impractical to obtain the model inputs, e.g. the snow's effective radius, on a global scale. Moreover, the emissivity spectra of snow/ice have an angle dependence, which currently cannot be well simulated by radiative transfer models (Hori et al. 2006; Cheng et al. 2010). We calculated the BBE of snow/ice using the emissivity spectra in the ASTER spectral library and the MODIS UCSB spectral library and found that 0.985 can be used as their BBE. The error is less than 0.005 when the viewing angle is less than 45°. For bare soils, transition areas, and vegetated areas, we computed their BBE by the DLNN. When the NDVI is less than 0.1 or larger than 0.2, their BBE was the same as that computed by the DLNN. The transition

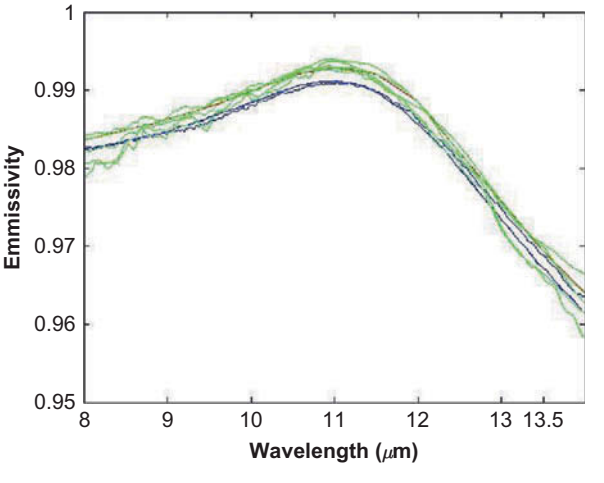

Figure 10. Comparison of the simulated pure water emissivity spectrum (red), the water emissivity spectra in the ASTER spectral library (blue), and the water emissivity spectra in the MODIS UCSB emissivity spectra (green).

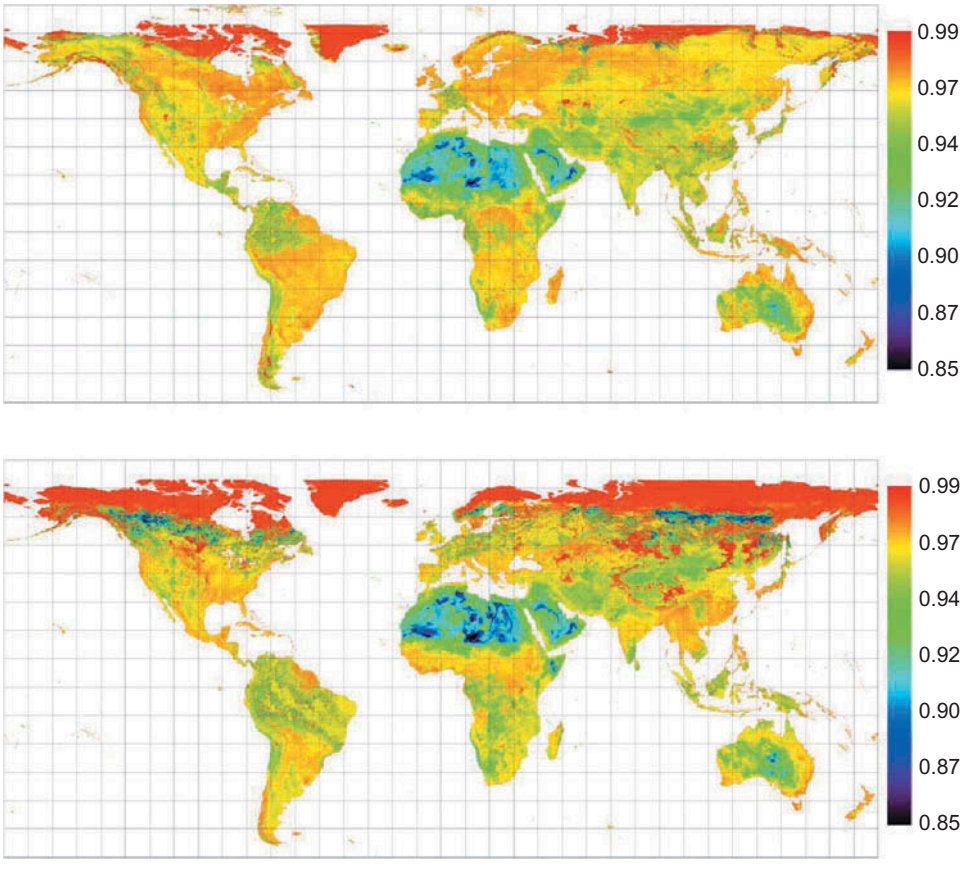

Figure 11. Global land-surface BBE on Julian day 145 (upper) and 321 (lower) in 2008.

areas were further divided into two parts based on the NDVI threshold: soil transition areas ($0.1 < \text{NDVI} \leq 0.156$) and vegetation transition areas ($0.156 < \text{NDVI} < 0.2$). For the soil transition areas, the BBE is the average of those computed by the DLNNs for the bare soils and the transition zone; in the vegetation transition areas, the BBE is the average value computed by the DLNNs for the transition zone and the vegetation. Figure 11 is an example of a generated 8 day 1 km global surface BBE in 2008.

7. Conclusions and discussion

The land-surface BBE is an essential parameter for estimating the surface longwave net radiation in the energy balance, ecosystem, and climate models. The BBE that was estimated from the satellite data has many unique merits and will contribute to land-surface energy balance studies and numerical weather predictions. In this study, we explored the non-linear relationship between the matched ASTER BBE and the MODIS albedos for bare soils, transition zones, and vegetated areas individually by using the DLNN. The DLNN was trained with a large number of samples that were extracted from relatively homogeneous and representative areas. The trained DLNN was tested using a group of samples that are independent of the training samples. The BBE that

was computed by the trained DLNN was consistent with that calculated from the ASTER narrowband emissivities. The bias and RMSE were $-1e^{-4}$ and 0.012 for bare soils, $2e^{-4}$ and 0.012 for transition areas, and $7e^{-4}$ and 0.010 for vegetated areas. The results indicate that the non-linear relationships established by the DLNN are significant and representative. The BBE that was computed by the DLNN for bare soils was validated by *in situ* measurements from seven dune sites. We also downloaded the spatial-temporal-matched ASTER emissivity and calculated the ASTER BBE. The computed BBE agreed well with the ASTER BBE, with an average difference of 0.007. The average difference between the computed BBE and the *in situ* BBE was 0.019. Ultimately, we introduced the strategy of generating a global land-surface BBE product and presented an example of a produced global BBE map. When the method was streamlined to generate an 8 day 1 km global surface BBE, the 8 day 500 m MODIS reflectance product (MOD09A1) will be aggregated into 1 km and then used to calculate a 1 km NDVI. Furthermore, all of the input data will be processed by another group within our team to ensure good data quality and spatial-temporal coverage. This processing will include cloud clearing, spatial-temporal filtering, and gap filling. Note that the aggregation of MOD09A1 data to 1 km will thus apply to the current MODIS albedo product (MCD43, Collection 5) because the MODIS science team will only provide albedos on a 500 m grid (MDC43A, Collection 6) in the future. We will update our algorithm and production scheme accordingly.

As can be seen from the test results and the validation results over bare soils, the developed DLNN can compute the BBE with an accuracy of better than 0.02. According to the study of Ogawa et al., the accuracy of the BBE retrieval from converting the ASTER narrowband emissivity is expected to be less than 0.02 (Ogawa and Schmugge 2004). Thus, the accuracy of the DLNN-computed BBE is comparable to that of the ASTER BBE. This acceptable accuracy of the BBE retrieval by the DLNN can benefit from two aspects: (1) the high accuracy in the ASTER emissivity and the MODIS albedo products. The primary goal of the ASTER TES algorithm is to compute the narrowband emissivity for the rocks and soils (Gillespie et al. 1998, 2011). The accuracy of the emissivity inversion for the rocks and soils is guaranteed. Some other validation studies show that the ASTER TIR emissivity achieved a high accuracy over arid and semi-arid areas (Hulley, Hook, and Baldridge 2009; Mira et al. 2011; Matsunaga et al. 2001; Sabol et al. 2009). Regarding the vegetation, the accuracy in the emissivity inversion cannot meet the design goal due to either having a low spectral contrast in the vegetation emissivity or being under high atmospheric temperatures and humidity, as reported by several authors (Jimenez-Munoz et al. 2006; Gillespie et al. 2011). When the TES algorithm was modified multiple times to accommodate the low emissivity contrasts and errors in the measured data, the accuracy was improved over the first version (Gustafson, Gillespie, and Yamada 2006). MODIS albedo has been extensively validated and is one of the most robust products in the remote-sensing community (Schaaf et al. 2002; Cescatti et al. 2012; Wang et al. 2012; Hulley, Hook, and Baldridge 2009; Román et al. 2009). (2) The DLNN established that the non-linear relationships between ASTER BBE and MODIS albedos are robust.

When compared with the BBE that was calculated from the MODIS narrowband emissivities that were computed by the day/night algorithm, the new BBE was found to possess the following obvious advantages. (1) *High spatial resolution.* The spatial resolution of the new BBE is 1 km, whereas the BBE calculated from the MODIS emissivity product has a resolution of approximately 5 km. A high-resolution net radiation product that includes the BBE has been required by many applications, such as irrigation

scheduling in agriculture. (2) *Product availability.* The MODIS day-night algorithm requires clear-sky conditions during both day and night (Wan and Li 1997). This requirement is strict and certainly results in many gaps in the computed emissivity products. (3) *Product accuracy.* The MODIS narrowband emissivities are determined by solving 14 variables in 14 equations (Wan and Li 1997), which makes them prone to measurement noise and could lead to local convergence (Gillespie et al. 1998; Peres and DaCamara 2006; Wan and Li 1997).

Because field measurements over vegetation canopies are rarely available, the computed BBE over the vegetated areas was not validated. There are several canopy emissivity models that can be used to model canopy emissivity as well as their BBE (Sobrino, Jimenez-Munoz, and Verhoef 2005; Snyder and Wan 1998). However, these models are not well validated by field measurements. More work on measuring the canopy emissivity at different spatial and temporal resolutions as well as the vegetation structure parameters should be conducted for the validation of surface emissivity retrieval algorithms and canopy emissivity models.

Theoretically, the hemispherical BBE is required to calculate surface longwave net radiation (Cheng and Liang 2014). The satellite emissivity has directionality because what the sensor measured is the radiance at a certain angle. In both the BBE calculated from the existing narrowband emissivity product and the BBE computed in this study, the directionality is neglected. The hemispherical BBE and the BBE at a certain angle are different in terms of both definition and magnitude. It is impractical to accumulate emissivity at different observational angles and then to calculate the hemispherical emissivity by integration. Meanwhile, the emissivity directional model is immature and lacks validation. Thus, it is difficult to derive hemispherical BBE at the current stage. An alternative approach is to improve and develop versatile physically based emissivity models that can characterize the emissivity angular distribution for typical land-surface types. With these models, we can either establish the relationship between hemispherical BBE and BBE at a certain angle or simulate the hemispherical BBE that is provided with surface characteristics.

Acknowledgements

We thank the anonymous referees for their constructive criticism and comments.

Funding

This work was supported by the National Natural Science Foundation of China [grant number 41371323]; the National High Technology Research and Development Programme of China [grant number 2013AA121201]; Beijing Youth Fellowship Programme [grant number YETP0233].

References

Aires, F., A. Chedin, N. A. Scott, and W. B. Rossow. 2002. "A Regularized Neural Net Approach for Retrieval of Atmospheric and Surface Temperatures with the IASI Instrument." *Journal of Applied Meteorology* 41: 144–159.

Baldridge, A. M., S. J. Hook, C. I. Grove, and G. Rivera. 2009. "The ASTER Spectral Library Version 2.0." *Remote Sensing of Environment* 113 (4): 711–715.

Baret, F., O. Hagolle, B. Geiger, P. Bicheron, B. Miras, M. Huc, B. Berthelot, F. Nino, M. Weiss, O. Semain, J.-L. Roujean, and M. Leroy. 2007. "LAI, fPAR, and fCover CYCLOPES Global

Products Derived from VEGETATION. Part 1: Principles of the Algorithm." *Remote Sensing of Environment* 110: 275–286.

Blackwell, W. J. 2005. "A Neural-Network Technique for the Retrieval of Atmospheric Temperature and Moisture Profiles from High Spectral Resolution Sounding Data." *IEEE Transactions on Geoscience and Remote Sensing* 43 (11): 2535–2546.

Bonan, G. B., K. W. Oleson, M. Vertenstein, S. Levis, X. Zeng, Y. Dai, R. E. Dickinson, and Z. Yang. 2002. "The Land Surface Climatology of the Community Land Model Coupled to the NCAR Community Climate Model." *Journal of Climate* 15: 3123–3149.

Born, M., and E. Wolf. 1999. *Principles of Optics: Electromagnetic Theory of Propagation, Interference, and Diffraction of Light*. 7th ed. Cambridge: Cambridge University Press.

Cescatti, A., B. Marcolla, S. K. Santhana Vannan, J. Y. Pan, M. O. Román, X. Yang, P. Ciais, R. B. Cook, B. E. Law, G. Matteucci, M. Migliavacca, E. Moors, A. D. Richardson, G. Seufert, and C. B. Scaaf. 2012. "Intercomparison of MODIS Albedo Retrievals and In Situ Measurements Across the Global FLUXNET Network." *Remote Sensing of Environment* 121: 323–334. doi:10.1016/j.rse.2012.02.019.

Chen, K. S., W. L. Kao, and Y. C. Tzeng. 1995. "Retrieval of Surface Parameters Using Dynamic Learning Neural Network." *International Journal of Remote Sensing* 16 (5): 801–809.

Chen, J., and S. Liang. 2013. "Estimating Global Land Surface Broadband Thermal-Infrared Emissivity Using Advanced Very High Resolution Radiometer Optical Data." *International Journal of Digital Earth* 6 (S1): 34–49.

Cheng, J., and S. Liang. 2014. "Effects of Thermal-Infrared Emissivity Directionality on Surface Broadband Emissivity and Longwave Net Radiation Estimation." *IEEE Geoscience and Remote Sensing Letters* 11 (2): 499–503.

Cheng, J., S. Liang, Q. Liu, and X. Li. 2011. "Temperature and Emissivity Separation From Ground-Based MIR Hyperspectral Data." *IEEE Transactions on Geoscience and Remote Sensing* 49 (4): 1473–1484.

Cheng, J., S. Liang, F. Weng, J. Wang, and X. Li. 2010. "Comparison of Radiative Transfer Models for Simulating Snow Surface Thermal Infrared Emissivity." *IEEE Journal of Selected Topics in Earth Observations and Remote Sensing* 3 (3): 323–336.

Cheng, J., S. Liang, Y. Yao, and X. Zhang. 2013. "Estimating the Optimal Broadband Emissivity Spectral Range for Calculating Surface Longwave Net Radiation." *IEEE Geoscience and Remote Sensing Letters* 10 (2): 401–405.

Cheng, J., Q. Liu, X. Li, Q. Xiao, Q. Liu, and Y.-M. Du. 2008. "Correlation-Based Temperature and Emissivity Separation Algorithm." *Science in China Series D: Earth Sciences* 51 (3): 363–372.

Cheng, J., Q. Xiao, X. Li, Q.-H. Liu, and Y.-M. Du. 2008. "Multi-Layer Perceptron Neural Network Based Algorithm for Simultaneous Retrieving Temperature and Emissivity From Hyperspectral FTIR Data." *Spectroscopy and Spectral Analysis* 28 (4): 780–783.

Fang, H., and S. Liang. 2003. "Retrieving Leaf Area Index with a Neural Network Method: Simulation and Validation." *IEEE Transactions on Geoscience and Remote Sensing* 41 (9): 2052–2062.

Fang, H., S. Wei, C. Jiang, and K. Scipal. 2012. "Theoretical Uncertainty Analysis of Global MODIS, CYCLOPES, and GLOBCARBON LAI Products Using a Triple Collocation Method." *Remote Sensing of Environment* 124: 610–621.

Gillespie, A. R., E. A. Abbott, L. Gilson, G. Hulley, J.-C. Jimenez-Munoz, and J. A. Sobrino. 2011. "Residual Errors in ASTER Temperature and Emissivity Products AST08 and AST05." *Remote Sensing of Environment* 115: 3681–3694.

Gillespie, A. R., S. Rokugawa, T. Matsunaga, J. S. Cothern, S. J. Hook, and A. B. Kahle. 1998. "A Temperature and Emissivity Separation Algorithm for Advanced Spaceborne Thermal Emission and Reflection Radiometer (ASTER) Images." *IEEE Transactions on Geoscience and Remote Sensing* 36: 1113–1126.

Gustafson, W. T., A. R. Gillespie, and G. J. Yamada. 2006. "Revisions to the ASTER Temperature/Emissivity Separation Algorithm." In *Second Recent Advances in Quantitative Remote Sensing*, edited by J. A. Sobrino, 770–775. Valencia: Publishion de la Universitat de Valencia. ISBN: 84-370-6533-5.

Hori, M., T. Aoki, T. Tanikawa, H. Motoyoshi, A. Hachikubo, K. Sugiura, T. J. Yasunari, H. Eide, R. Storvold, Y. Nakajima, and F. Takahashi. 2006. "In-Situ Measured Spectral Directional Emissivity of Snow and Ice in the 8–14 um Atmospheric Window." *Remote Sensing of Environment* 100: 486–502.

Hornik, K. M., M. Stinchcombe, and H. White. 1989. "Multilayer Feedforward Networks Are Universal Approximators." *Neural Networks* 4 (5): 359–366.

Hulley, G. C., S. J. Hook, and A. M. Baldridge. 2009. "Validation of the North American ASTER Land Surface Emissivity Database (NAALSED) Version 2.0 Using Pseudo-Invariant Sand Dune Sites." *Remote Sensing of Environment* 113: 2224–2233.

Jacob, F., F. Petitcolin, T. Schmugge, E. Vermote, A. French, and K. Ogawa. 2004. "Comparison of Land Surface Emissivity and Radiometric Temperature Derived from MODIS and ASTER Sensors." *Remote Sensing of Environment* 90 (2): 137–152.

Jimenez-Munoz, J. C., J. A. Sobrino, A. Gillespie, D. Sabol, and W. T. Gustafson. 2006. "Improved Land Surface Emissivities over Agricultural Areas Using ASTER NDVI." *Remote Sensing of Environment* 103 (4): 474–487.

Jin, M., and S. Liang. 2006. "An Improved Land Surface Emissivity Parameter for Land Surface Models Using Global Remote Sensing Observations." *Journal of Climate* 19: 2867–2881.

Jin, Y., and C. Liu. 1997. "Biomass Retrieval from High-Dimensional Active/Passive Remote Sensing Data by Using Artificial Neural Network." *International Journal of Remote Sensing* 18 (4): 971–979.

Li, Z.-L., H. Wu, N. Wang, S. Qiu, J. A. Sobrino, Z.-M. Wan, B.-H. Tang, and G.-J. Yan. 2013. "Land Surface Emissivity Retrieval From Satellite Data." *International Journal of Remote Sensing* 34 (9–10): 3084–3127.

Liang, S. 2004. "Estimation of Surface Radiation Budget: II. Longwave." In *Quantitative Remote Sensing of Land Surface*, edited by J. A. Kong, 378. Hoboken, NJ: John Wiley and Sons.

Liang, S. 2011. "Review on Estimation of Land Surface Radiation and Energy Budgets from Ground Measurement, Remote Sensing and Model Simulations." *IEEE Journal of Selected Topics in Applied Earth Observations and Remote Sensing* 3: 225–240.

Liang, S., K. Wang, X. Zhang, and M. Wild. 2010. "Review of Estimation of Land Surface Radiation and Energy Budgets from Ground Measurements, Remote Sensing and Model Simulation." *IEEE Journal of Selected Topics in Earth Observations and Remote Sensing* 3 (3): 225–240.

Liou, Y.-A., Y. C. Tzeng, and K. S. Chen. 1999. "A Neural-Network Approach to Radiometric Sensing of Land-Surface Parameters." *IEEE Transactions on Geoscience and Remote Sensing* 37 (6): 2718–2724.

Mao, K., J. Shi, H. Tang, Z.-L. Li, X. Wang, and K.-S. Chen. 2008. "A Neural Network Technique for Separating Land Surface Emissivity and Temperature from ASTER Imagery." *IEEE Transactions on Geoscience and Remote Sensing* 46 (1): 200–208.

Matsunaga, T., Y. Sawabe, S. Rokugawa, H. Tonooka, and M. Moriyama. 2001. "Early Evaluation of ASTER Emissivity Products and Its Application to Environmental and Geologic Studies." *Proceedings of SPIE* 4486: 20–30. doi:10.1117/12.455121.

Mira, M., T. J. Schmugge, E. Valor, V. Caselles, and C. Coll. 2011. "Analysis of ASTER Emissivity Product over an Arid Area in Southern New Mexico, USA." *IEEE Transactions on Geoscience and Remote Sensing* 49 (4): 1316–1324.

Momeni, M., and M. R. Saradjian. 2007. "Evaluating NDVI-Based Emissivities of MODIS Bands 31 and 32 Using Emissivities Derived by Day/Night LST Algorithm." *Remote Sensing of Environment* 106 (2): 190–198.

Ogawa, K., and T. Schmugge. 2004. "Mapping Surface Broadband Emissivity of the Sahara Desert Using ASTER and MODIS Data." *Earth Interactions* 8: 1–14.

Ogawa, K., T. Schmugge, F. Jacob, and A. Prench. 2002. "Estimation of Broadband Land Surface Emissivity from Multi-Spectral Thermal Infrared Remote Sensing." *Agronomie* 22: 695–696.

Ogawa, K., T. Schmugge, and S. Rokugawa. 2008. "Estimating Broadband Emissivity of Arid Regions and Its Seasonal Variations Using Thermal Infrared Remote Sensing." *IEEE Transactions on Geoscience and Remote Sensing* 46 (2): 334–343.

Peres, L. F., and C. C. DaCamara. 2006. "Improving Two-Temperature Method Retrievals Based on a Nonlinear Optimization Approach." *IEEE Geoscience and Remote Sensing Letters* 3 (2): 232–236.

Ren, H., S. Liang, G. Yan, and J. Cheng. 2013. "Empirical Algorithms to Map Global Broadband Emissivities over Vegetated Surfaces." *IEEE Transactions on Geoscience and Remote Sensing* 51 (5): 2619–2631. doi:10.1109/TGRS.2012.2216887.

Román, M. O., C. B. Schaaf, C. E. Woodcock, A. H. Strahler, X. Yang, R. H. Braswell, P. S. Curtis, K. J. Davis, D. Dragoni, M. L. Goulden, L. Gu, D. Y. Hollinger, T. E. Kold, T. P. Meyers, J. W. Munger, J. L. Privette, A. D. Richardson, T. B. Wilson, and S. C. Wofsy. 2009. "The MODIS (Collection V005) BRDF/Albedo Product: Assessment of Spatial Representativeness over Forested Landscapes." *Remote Sensing of Environment* 113 (11): 2476–2498. doi:10.1016/j.rse.2009.07.009.

Sabol, D. E. Jr., A. R. Gillespie, E. Abbott, and G. Yamada. 2009. "Field Validation of the ASTER Temperature-Emissivity Separation Algorithm." *Remote Sensing of Environment* 113: 2328–2344.

Schaaf, C. B., F. Gao, A. H. Strahler, W. Lucht, X. Li, T. Tsang, N. C. Strugnell, X. Zhang, Y. Jin, J.-P. Muller, P. Lewis, M. Barnsley, P. Hobson, M. Disney, G. Roberts, M. Dunderdale, C. Doll, R. P. d'Entermont, B. Hu, S. Liang, J. L. Privette, and D. Roy. 2002. "First Operational BRDF, Albedo Nadir Reflectance Products from MODIS." *Remote Sensing of Environment* 83: 135–148.

Schmugge, T., A. French, J. C. Ritchie, A. Rango, and H. Pelgrum. 2002. "Temperature and Emissivity Separation from Multispectral Thermal Infrared Observations." *Remote Sensing of Environment* 79 (2–3): 189–198. doi:10.1016/s0034-4257(01)00272-3.

Sellers, P. J., R. E. Dickinson, D. A. Randall, A. K. Betts, F. G. Hall, J. A. Berry, G. J. Collatz, A. S. Denning, H. A. Mooney, C. A. Nobre, N. Sato, C. B. Field, and A. Henderson-Selles. 1997. "Modeling the Exchange of Energy, Water and Carbon Between the Continents and the Atmosphere." *Science* 275: 502–509.

Smith, J. A. 1993. "LAI Inversion Using a Back-Propagation Neural Network Trained with a Multiple Scattering Model." *IEEE Transactions on Geoscience and Remote Sensing* 31: 1102–1106.

Snyder, W. C., and Z. Wan. 1998. "BRDF Models to Predict Spectral Reflectance and Emissivity in the Thermal Infrared." *IEEE Transactions on Geoscience and Remote Sensing* 36: 214–225.

Sobrino, J. A., J. C. Jimenez-Munoz, and W. Verhoef. 2005. "Canopy Directional Emissivity: Comparison Between Models." *Remote Sensing of Environment* 99: 304–314.

Tang, B.-H., H. Wu, C. Li, and Z.-H. Li. 2011. "Estimation of Broadband Surface Emissivity From Narrowband Emissivities." *Optical Express* 19 (1): 185–192.

Tang, L., Z. Chen, S. Oh, R. J. Marks, and A. T. C. Chang. 1992. "Inversion of Snow Parameters from Passive Microwave Remote Sensing Measurements by a Neural Network Trained with a Multiple Scattering Model." *IEEE Transactions on Geoscience and Remote Sensing* 30 (5): 1015–1024.

Tedesco, M., J. Pulliainen, M. Takala, M. Hallikainen, and P. Pampaloni. 2004. "Artificial Neural Network-Based Techniques for the Retrieval of SWE and Snow Depth From SSM/I Data." *Remote Sensing of Environment* 90 (1): 76–85.

Tsvetsinskaya, E. A., C. B. Schaaf, F. Gao, A. H. Strahler, R. E. Dickinson, X. Zeng, and W. Lucht. 2002. "Relating MODIS-Derived Surface Albedo to Soils and Rock Types over Northern Africa and Arabian Peninsula." *Geophysical Research Letters* 29 (9): 67-1–67-4. doi:10.1029/2001GL014096.

Turquety, S., J. Hadji-Lazaro, and C. Clerbaux. 2002. "First Satellite Ozone Distributions Retrieved from Nadir High-Resolution Infrared Spectra." *Geophysical Research Letters* 29 (24): 51-1–51-4. doi:10.1029/2002GL016431.

Tzeng, Y. C., K. S. Chen, W. L. Kao, and A. K. Fung. 1994. "A Dynamic Learning Neural Network for Remote Sensing Applications." *IEEE Transactions on Geoscience and Remote Sensing* 32: 1096–1102.

Wan, Z., and Z.-L. Li. 1997. "A Physics-Based Algorithm for Retrieving Land-Surface Emissivity and Temperature from EOS/MODIS Data." *IEEE Transactions on Geoscience and Remote Sensing* 35 (4): 980–996.

Wang, K., Z. Wan, P. Wang, M. Sparrow, J. Liu, X. Zhou, and S. Haginoya. 2005. "Estimation of Surface Long Wave Radiation and Broadband Emissivity Using Moderate Resolution Imaging Spectroradiometer (MODIS) Land Surface Temperature/Emissivity Products." *Journal of Geophysical Research* 110: D11109. doi:10.1029/2004JD005566.

Wang, Z., C. B. Schaaf, M. J. Chopping, A. H. Strahler, J. Wang, M. O. Román, A. V. Rocha, C. E. Woodcock, and Y. Shuai. 2012. "Evaluation of Moderate-Resolution Imaging Spectroradiometer (MODIS) Snow Albedo Product (MCD43A) over Tundra." *Remote Sensing of Environment* 117: 264–280. doi:10.1016/j.rse.2011.10.002.

Wilber, A. C., D. P. Kratz, and S. K. Gupta. 1999. "Surface Emissivity Maps for Use in Satellite Retrievals of Longwave Radiation." Hampton, VA: NASA Technical Publications, NASA/TP-1999-209362.

Zhou, L., R. E. Dickinson, K. Ogawa, Y. Tian, M. Jin, T. Schmugge, and E. Tsvetsinskaya. 2003. "Relations Between Albedos and Emissivities from MODIS and ASTER Data over North African Desert." *Geophysical Research Letters* 30 (20): 2026. doi:10.1029/2003GL018069.

Zhou, L., R. E. Dickinson, Y. Tian, M. Jin, K. Ogawa, H. Yu, and T. Schmugge. 2003. "A Sensitivity Study of Climate and Energy Balance Simulations with Use of Satellite-Based Emissivity Data over Northern Africa and the Arabian Peninsula." *Journal of Geophysical Research* 108 (D24): 4795. doi:10.1029/2003JD004083.